Electronic Supplementary Material (ESI) for Catalysis Science & Technology.

The Influence of Solvent Composition on the Coordination Environment of the Co/Mn/Br based *para*-Xylene Oxidation Catalyst as reveraled by EPR and ESEEM Spectroscopy

Rebekah L. Taylor,*[a] Duncan Housley,[b] Michael Barter,[c] Adrian Porch,[c] Keith Whiston,[b] Andrea Folli*[a] and Damien M. Murphy [a]

[a] School of Chemistry, Cardiff University, Main Building, Park Place, Cardiff, CF10 3AT
[b] Koch Technology Solutions Ltd., The Wilton Centre, Wilton, Redcar, TS10 4RE
[c] School of Engineering, Cardiff University, The Parade, Cardiff CF24 3AA, UK.

CONTENTS

1. Methods

Sample Preparation

All reagents were purchased from Sigma Aldrich and used without further purification. For CW EPR and UV-vis spectroscopies, ternary systems of $Co(OAc)_2$, $Mn(OAc)_2$ and NaBr (hereafter simply referred to as Co/Mn/Br) were employed. Specifically, $Co(OAc)_2$ (17.75 mM), $Mn(OAc)_2$ (17.75 mM) and NaBr (35.5 mM) were dissolved in H_2O and glacial acetic acid (AcOH) mixtures at different ratios, ranging from 0 wt% to 20 wt% of H_2O.

For pulse EPR measurements, a binary system (hereafter referred to as Mn/Br) composed of $Mn(OAc)_2$ (35.5 mM) and NaBr (35.5 mM) dissolved in H_2O and glacial AcOH mixtures was used with varying water content; i.e., 3 wt%, 8 wt%, 13.7 wt% and 20 wt% H_2O. Mn(DTPA) (where DTPA refers to the ligand diethylenetriaminepentaacetic acid, $Na_5DTPA.5H_2O$) samples were prepared at the same solvent compositions by dissolving $MnCl_2.4H_2O$ (35.5 mM) and $Na_5DTPA.5H_2O$ (177.5 mM) in the corresponding H_2O and glacial AcOH mixture. $Mn(H_2O)_6^{2+}$ was prepared by dissolving $MnCl_2.4H_2O$ (35.5 mM) with sucrose (1.5 and 1.9 M) in H_2O. The same set of samples for pulse EPR measurements were also prepared in D_2O by dissolving the as-purchased reagents in D_2O and drying in vacuo three times. This was performed to ensure that no H_2O was present in the reagents that were then used to prepare the D_2O/AcOH-based samples.

Electron Paramagnetic Resonance (EPR) Spectroscopy

X-band Continuous Wave (CW) EPR spectra were recorded on a Bruker EMX spectrometer operating at 100 kHz field modulation frequency, 0.3 mT field modulation amplitude and 2 mW microwave power in a high sensitivity resonator (Bruker ER-4122 SHQE) at 363 K. 150 µl of sample was loaded into a quartz Q-band EPR tube (1.6 mm internal diameter) and sealed with PTFE tape to prevent any loss of sample by evaporation. Samples were left in the preheated resonator to thermally equilibrate at the desired temperature before recording the EPR spectra.

The high-pressure cell for X-band High Pressure EPR used in this work is the commercially available yttria-stabilised zirconia ceramic cell (HIB440-Cer; Pressure BioSciences, Inc.) total volume *ca*. 18 µl with *ca*. 5 µl in the active region of the resonator. A schematic of the cell is shown in S1. The cell was interfaced to the HUB440 pressure intensifier (Pressure BioSciences, Inc.) which operated within an applied (output) pressure range 0-2000 bar. A Bruker MEX EPR spectrometer equipped with a Bruker ER-4119 HS resonator were employed for EPR measurements with the HUB440-Cer cell inserted in the top of the resonator.

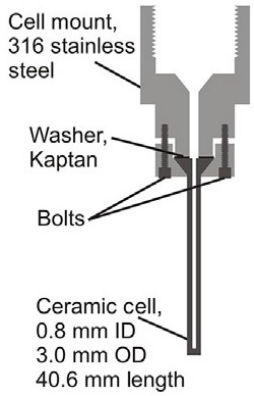

S1 – Schematic of the Pressure BioScience HUB440-Cer cell for high pressure EPR of liquid samples attached to the pressure mount that connects to the HUB440 pressure intensifier (not shown here).

Three-pulse Electron Spin Echo Envelope Modulation (ESEEM) measurements were performed on a Bruker ELEXSYS E580 spectrometer operating at X-band frequency fitted with a Bruker EN 4118X-MD4. The measurements were performed at 5 K using the following pulse sequence $\pi/2$-τ-$\pi/2$-T-$\pi/2$-*echo*, with $t_{\pi/2}$ = 16 ns, T = 400 ns (256 time intervals) and τ = 200 ns. τ was chosen to be a multiple integer of the ^{1}H precession period at 349.8 mT to decouple any ^{1}H modulation, and τ was increased by 200 ns for the same reason. For the measurements, 150 µl of sample was used in a X-band quartz tube (3 mm internal diameter).

ESEEM time profiles were processed using the method described by Hoogstraten and Britt.[1] Briefly, three-pulse ESEEM time profiles were normalised for corresponding ^{1}H and ^{2}H data with respect to the maximum of the first modulation in the ^{2}H spectrum and noise filtered by performing a level 3 wavelet decomposition of the signal and denoising it using Donoho and Johnstone's universal threshold with level-dependent estimation of the noise. Denoised versions were obtained using the maximal overlap discrete wavelet transform (MODWT) with soft thresholding. ^{2}H/^{1}H ratios of the spectra were taken and multiplied by an exponential or rational growth or decay to remove any artefacts arising from discrepancies in relaxation between samples where required. The resulting analyte and Mn(DTPA) data were again renormalised, ^{2}H/^{1}H ratios taken, and relaxation artefact removed where required. The process was repeated for $Mn(H_2O)_6^{2+}$, and the intensity was scaled to account for different number of D_2O ligands by raising the intensity to the power of (N/6), where N= 1-6 represents the number of D_2O ligands.

Viscosity Measurements

The viscosity of the different H_2O/AcOH mixtures investigated in this study was measured using a Rheoltek U-Tube viscometer size B at *ca*. 293, 333 and 353 K. The solvent was brought to temperature by placing the viscosimeter in a water bath until thermal equilibrium was reached before recording the viscosity. The solvent density was determined by weighing the mass of 10.00 ml of solvent heated to temperature.

UV-vis Spectroscopy

Room temperature UV-vis spectra were recorded on a Shimadzu UV-2401PC spectrometer using 1 cm matched quartz cuvettes at room temperature. Variable temperature UV-vis spectra were recorded using an EEPROM USB2 model dip-probe by Anglia Instruments connected to a Shimadzu UV-2401PC spectrometer

Dielectric permittivity measurements

The broadband, microwave spectra of liquids were conveniently measured using an open-ended coaxial probe.[2] The complex microwave permittivity measurements of acetic acid/water mixtures were measured using the method outlined in.[3] The coaxial probe was manufactured in-house, by first mechanically milling the end of a square SMA panel mount connector (Amphenol RF, 901-9892-RFX), followed by polishing to form a flat coaxial aperture of inner diameter 1.25 mm, outer diameter 4.1 mm, with a PTFE dielectric spacer of relative permittivity 2.05 and negligible dielectric loss. Details of the probe are shown in the photograph of S2a. Its relatively large aperture size makes it unsuitable for measurements above 5 GHz, owing to excessive radiation losses into the sample space and the simplicity of the capacitive model used to extract complex permittivity. It is also unsuitable below 10 MHz, where random errors in the real part of the complex permittivity are very large due to the tiny electrical phase differences measured. However, the 10 MHz – 5 GHz bandwidth is the most valuable for studying dielectric dispersion and relaxation processes in aqueous acetic acid and allows

reliable extrapolation to very low frequencies to infer static dielectric constants and ionic conductivities.

a)

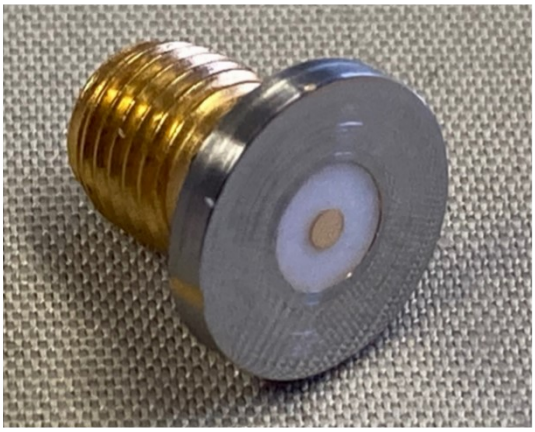

b)

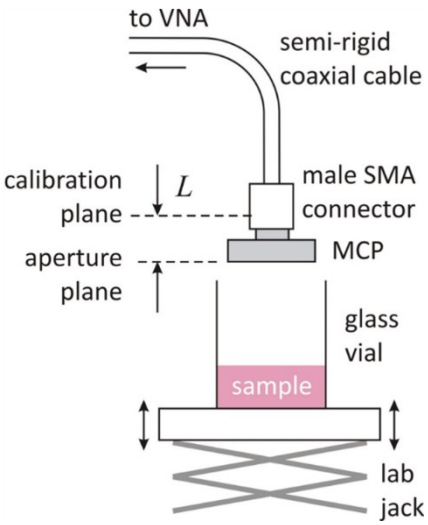

S2 - a) Photograph of the SMA connector, adapted for use as a broadband dielectric probe for the measurements presented here; the aperture diameter is 4.1 mm, with a center conductor of diameter 1.25 mm. b) A schematic diagram of the experimental setup; the length L between the aperture and calibration plane is kept as short as possible by using this connector and is removed in the analysis by normalising all voltage reflection (S_{11}) measurements by those of the air-terminated probe.[3]

The coaxial probe was dipped directly into the liquids under test, which were contained in glass vials filled to a depth of around 2 cm (see Fig. S2b). For measurements at 363 K, dip tests were performed with the sample on a hot plate, waiting for the probe to reach thermal equilibrium with each sample. Microwave measurements of the probe's voltage reflection coefficient S_{11} were performed using a vector network analyser (VNA, Keysight N5232A). The probe was carefully calibrated to obtain reliable complex permittivity measurements and all calibrations were performed at room temperature (298 K). A one-port mechanical calibration was performed using the short, open and load standards from a coaxial calibration kit (Keysight 85033E), thus defining a calibration plane for S_{11} at the probe's SMA connector interface. The probe's electrical length was corrected from the calibration plane to the aperture (i.e., sample) plane by normalizing the S_{11} data at each frequency to those of an air-terminated probe,[3] held a few cm above the liquid. A simple capacitive model[3] was used for the admittance of the coaxial aperture $Y = i\omega\varepsilon A$ at each frequency $\omega = 2\pi f$ to calculate the liquid's complex permittivity $\varepsilon = \varepsilon_1 - i\varepsilon_2$. The frequency-independent, geometrical constant *A* is determined from measurements of a known, standard polar liquid. We choose methanol since it has very well-established complex permittivity values (well-described by the Debye model),[4] which are similar in values to the complex permittivities of the acetic acid/water mixtures measured here (i.e. 6 to 37). The experimentally determined value is A = 1.50 ± 0.03 x 10^{-12} s/Ω, which is in good agreement with the value A = 1.55 ± 0.03 x 10^{-12} s/Ω calculated theoretically for a coaxial aperture of the same dimensions, but with an infinite ground plane.

2. EPR spectra at 296 K

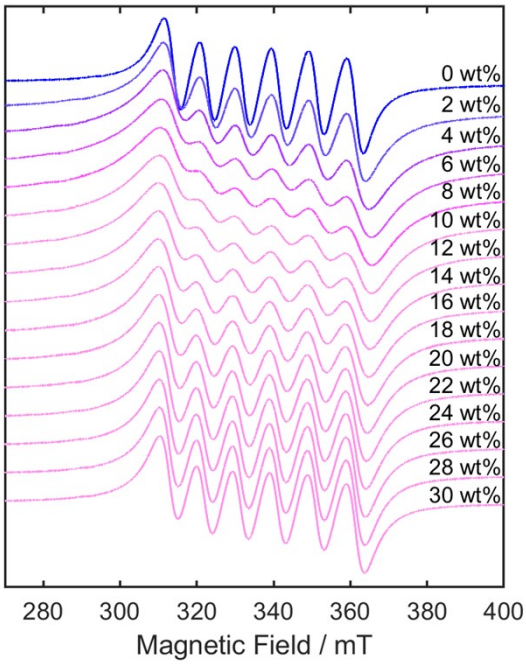

S3 – CW X-band EPR spectra of the Co/Mn/Br catalyst in varying wt% H_2O solvent compositions, recorded at 296 K.

The choice of the m_I = +1/2 transitions for the lwpp analysis presented in Fig. 1b in the main text was made on the basis that these lines were shown to be the least affected by relaxation and unresolved superhyperfine interactions,[5,6] and therefore better represent any real changes in lwpp arising from other sources.

3. CW EPR control experiments

a) Temperature

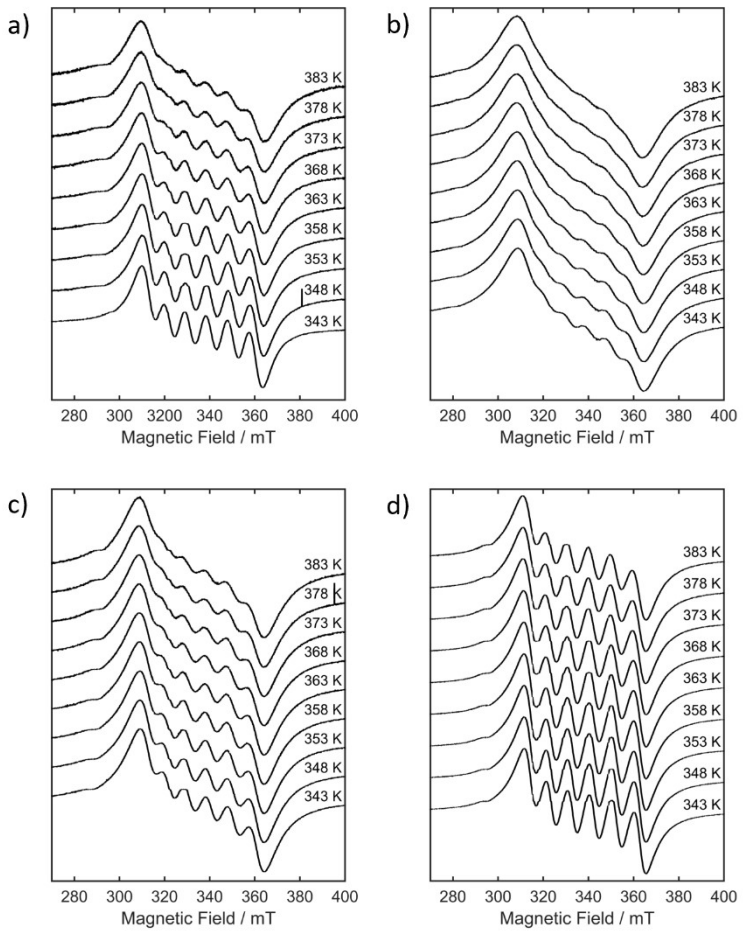

S4 – Variable temperature CW X-band EPR spectra of the Co/Mn/Br catalyst in H_2O/AcOH compositions of a) 3 wt%, b) 8 wt%, c) 13.7 wt% and d) 20 wt%.

The temperature of the measurements in Fig. 2a of the main text and Fig. S3 were produced with an error of < ± 0.2 K. Here, temperatures of at least ± 2 K were required to cause lwpp changes of 0.3 mT, not consistent with the magnitude of change observed in the main text at a smaller temperature fluctuation. These lwpp changes were found to be as a result of differing rates of chemical exchange (as discussed in the main text), and have been observed in other Mn^{2+} systems previously.[7-9]

b) Concentration

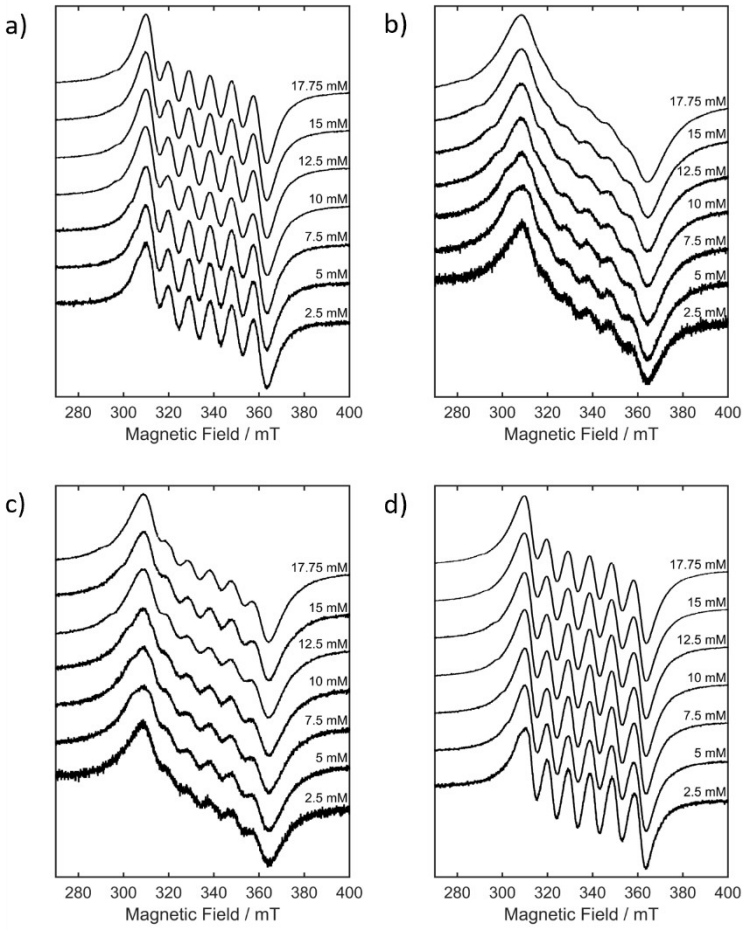

S5 – CW X-band EPR spectra of the Co/Mn/Br catalyst in H_2O/AcOH compositions of a) 3 wt%, b) 8 wt%, c) 13.7 wt% and d) 20 wt%.

The experimental method used to produce the data in Fig. 2a in the main text required sequential dilution of the catalytic system with H_2O to maintain the exact same Co/Mn/Br ratio with changing H_2O/AcOH ratio. To exclude concentration broadening as the cause of the changing lwpp over this solvent composition range, the Co/Mn/Br catalyst was diluted with a fixed H_2O/AcOH ratio beyond the range of concentrations achieved in the main text (5 mM). A dilution of > 15 mM was found not to affect the Mn^{2+} lwpp under the same conditions, enabling us to dismiss concentration broadening as the cause of the lwpp changes under our experimental conditions.

c) Variable Pressure

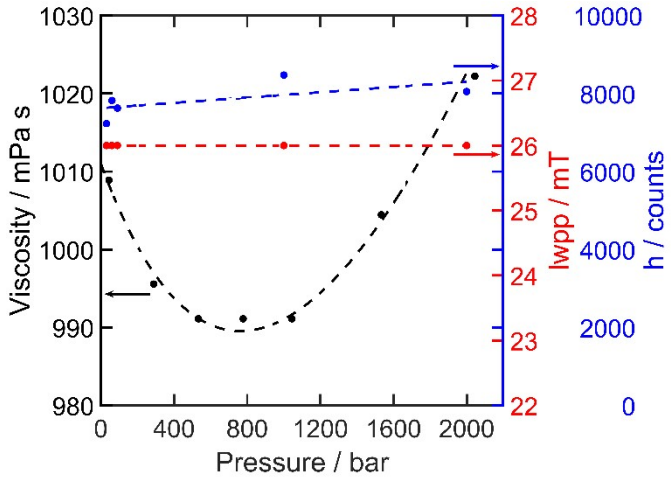

S6 - EPR linewidth (red) and signal amplitude (blue) measured from the data presented in Fig. 1d (main text) plotted as a function of pressure and the corresponding reported H_2O viscosity (black), as presented in Fig. 1 in the main text.

The m_I = +1/2 linewidth of the Mn^{2+} signal shows no variation over the pressure range of 30 – 2000 mPa s as would be expected due to the rotational averaging in solution not significantly contributing to the relaxation of the system,[10,11] and thus the linewidth with changing viscosity. However, the signal amplitude does exhibit a slight increase with pressure caused by a slight increase in effective spin concentration in the active part of the resonator as the sample is compressed.

4. Microwave Permittivity

Results for the complex permittivity of acetic acid/water mixtures for wt% water content in the range 0 wt% to 20 wt% are shown in S5, at 298 K and 363 K, respectively. For glacial acetic acid (0 wt% H_2O), the results at 298 K for the imaginary permittivity ε_2 exhibit a loss peak (a characteristic of polar liquids) centred around 1.7 GHz, with an associated dispersion in ε_1 which has an extrapolated static value of 6.6 ± 0.2. Increased wt% H_2O increases the static permittivity ε_2 greatly (as expected owing to the highly polar nature of water molecules) but has little relative effect on the loss peak. The main effect on ε_2 is the appearance of the rapidly increasing loss term at low frequencies due to the increasing static ionic conductivity σ as a result of the increasing concentration of acetate and hydronium ions, with $\varepsilon_2 \approx \sigma/\varepsilon_0\omega$ in this low frequency limit.

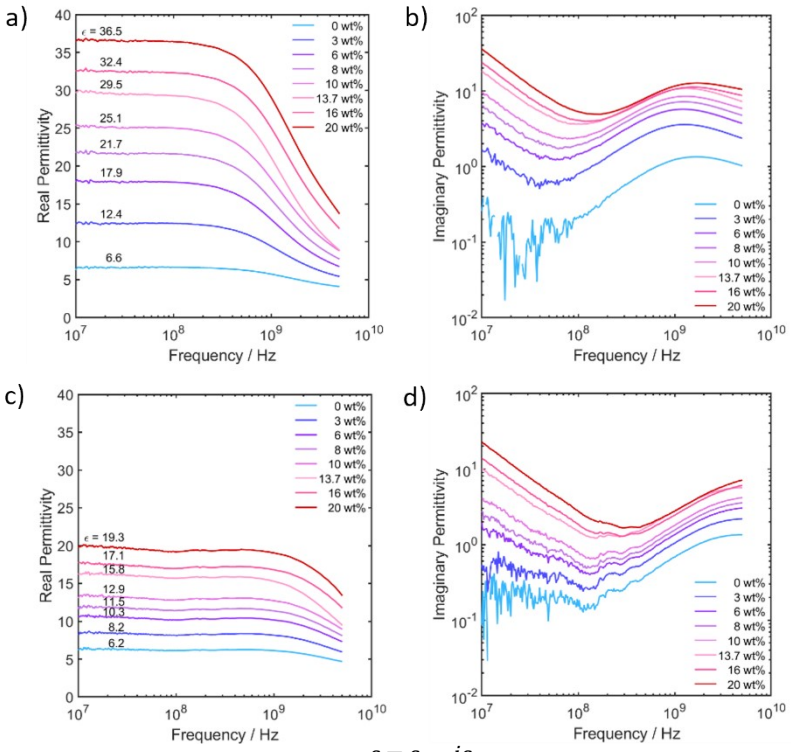

S7 – Real and imaginary parts of the complex permittivity $\varepsilon = \varepsilon_1 - i\varepsilon_2$ of acetic acid in water at a) 298 K and c) 363 K over the frequency range 10 MHz – 5 GHz, plotted for different wt% H_2O content. The upturn in ε_2 at low frequencies is due to the ionic conductivity σ of the solution, which increases on increasing wt% H_2O. Error bars are not shown, but random errors are negligible compared with the systematic error of ± 2 % and ± 4 % at 298 and 363 K respectively, associated with the capacitive model to extract the data and the fact that the microwave measurement calibration was performed at 298 K for all data sets.

There are very few literature reports of microwave dielectric spectroscopy of concentrated acetic acid at 298 K,[12,13] with none published (to our knowledge) at elevated temperatures. Our results at 298 K are in very good agreement with Kaatze *et al.*,[14] where the microwave dielectric spectrum of concentrated acetic acid was modelled using the Davidson-Cole model,[14,15] expressed in eq. 1 below. This is an empirical extension of the Debye model for polar materials exhibiting a range of dipole relaxation times, characteristics of which are asymmetric loss peaks in ε_2 (when plotted logarithmically) and non-semicircular ("teardrop" shaped) Cole-Cole plots of complex permittivity.

$$\varepsilon(\omega,T) = \varepsilon_\infty(T) + \frac{\varepsilon_s(T) - \varepsilon_\infty(T)}{\left(1 + i\omega\tau_{DC}(T)\right)^{1-\beta(T)}} - i\frac{\sigma(T)}{\varepsilon_0\omega} \qquad \text{(eq. 1)}$$

In eq. 1, the complex permittivity has been appended by the (static) ionic conductivity term and all temperature dependent terms have been made explicit; τ_{DC} is the Davidson-Cole relaxation time, a characteristic value representative of a spread of relaxation times, β is a frequency-independent constant and ε_s, ε_∞ are the (real) permittivities in the static and very high frequency limits, respectively.

Table 1 - Dielectric parameters extracted from the complex permittivity data of acetic acid/water mixtures at 298 K by fitting to the Davidson-Cole model (all other parameters are defined in eq. 1).

wt% H_2O	σ μS/cm	ε_∞	ε_s	τ_{DC} / ps	β
0	1.27 ± 0.03	2.8 ± 0.1	6.6 ± 0.1	170 ± 10	0.52 ± 0.02
3	9.88 ± 0.20	2.9 ± 0.1	12.5 ± 0.3	205 ± 12	0.46 ± 0.02
6	21.9 ± 0.4	3.0 ± 0.1	18.0 ± 0.4	210 ± 12	0.44 ± 0.02
8	37.9 ± 0.8	3.3 ± 0.1	21.8 ± 0.4	200 ± 12	0.42 ± 0.02
10	56.8 ± 1.1	3.3 ± 0.1	25.3 ± 0.5	190 ± 11	0.42 ± 0.02
13.7	108 ± 2	3.4 ± 0.1	29.7 ± 0.6	170 ± 10	0.42 ± 0.02
16	141 ± 3	3.3 ± 0.1	32.7 ± 0.7	155 ± 9	0.43 ± 0.02
20	213 ± 4	3.3 ± 0.1	36.9 ± 0.7	145 ± 9	0.44 ± 0.02

Table 2 - Dielectric parameters extracted from the complex permittivity data of acetic acid/water mixtures at 363 K by fitting to the Davidson-Cole model (all other parameters are defined in eq. 1).

wt% H_2O	σ μS/cm	ε_∞	ε_s	τ_{DC} / ps	β
0	0.76 ± 0.03	2.4 ± 0.1	6.3 ± 0.3	65 ± 6	0.54 ± 0.02
3	3.00 ± 0.12	2.0 ± 0.1	8.5 ± 0.3	63 ± 6	0.56 ± 0.02
6	10.1 ± 0.4	1.8 ± 0.1	10.5 ± 0.4	57 ± 5	0.54 ± 0.02
8	15.0 ± 0.6	1.8 ± 0.1	11.8 ± 0.5	57 ± 5	0.54 ± 0.02
10	23.5 ± 0.9	1.8 ± 0.1	13.2 ± 0.5	55 ± 5	0.52 ± 0.02
13.7	59.2 ± 2.4	1.7 ± 0.1	16.1 ± 0.6	50 ± 5	0.50 ± 0.02
16	80.5 ± 3.2	1.6 ± 0.1	17.4 ± 0.7	48 ± 5	0.49 ± 0.02
20	132 ± 5	1.6 ± 0.1	19.7 ± 0.8	45 ± 5	0.48 ± 0.02

Cole-Cole plots of the complex permittivity data of Fig. S6 are shown in Fig. S7. From this data, Davidson-Cole modelling using eq. 1 has been used to extract the material parameters listed in Tables 1 and 2, at temperatures of 298 K and 363 K respectively. At 298 K, on increasing the wt% H_2O content there are large increases in both the static permittivity ε_s and static ionic conductivity σ, with relatively much smaller changes in the other material parameters, including τ_{DC}. Comparing the glacial (0 wt% H_2O) acetic acid data at 298 K and 363 K, the largest change is the increased frequency of the loss peak, from around 1.7 GHz to just below 5 GHz. This is linked to a large decrease in τ_{DC}, from 170 ± 10 ps at 298 K to 65 ± 5 ps at 363 K, but with relatively much smaller (< 10 %) decreases in both ε_s and ε_∞. As at 298 K, increasing the wt% H_2O content at 363 K results again in large increases in both ε_s and σ (though not as large as those observed at 298 K), with little change in other material properties.

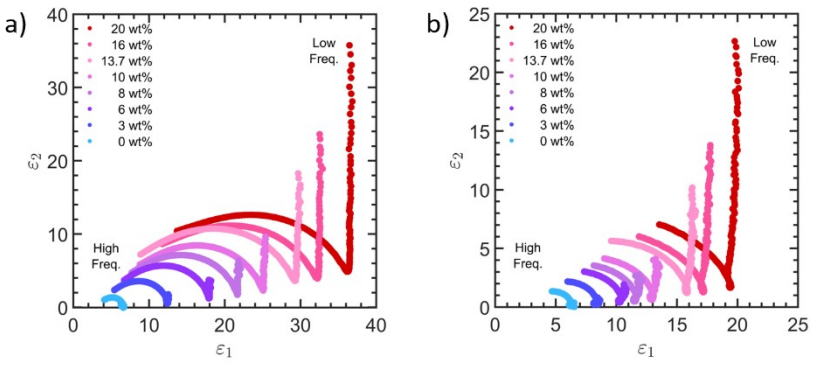

S8 – Cole-Cole plots of the complex permittivity $\varepsilon = \varepsilon_1 - i\varepsilon_2$ of acetic acid in water at a) 298 K and b) 363 K over the frequency range 10 MHz – 5 GHz, plotted for different wt% H_2O content. Davidson-Cole modelling of this data is used to obtain the parameters of Tables 1 and 2. The effect of ionic conductivity is clear at the low frequency ends (i.e. right hand ends) of each plot. Error bars are not shown but there is a systematic error of ± 2 % and ± 4 % in both real and imaginary parts for 298 and 363 K respectively.

The static permittivity ε_s and static conductivity σ, respectively, taken from Tables 1 and 2 as functions of wt% water are plotted in S8. Both vary non-linearly with wt% at each temperature and for fixed wt% both are reduced in value at the higher temperature (expected behavior for ε_s for a polar liquid); indeed, ε_s becomes more sensitive to temperature for greater wt% H_2O content, to be expected owing to the highly temperature dependent dielectric properties (of ε_1 in particular) of pure water. The static conductivity σ is also reduced at the higher temperature for the same wt%, which is most likely due to the reduced ionic mobility owing to a reduced ionic scattering time.

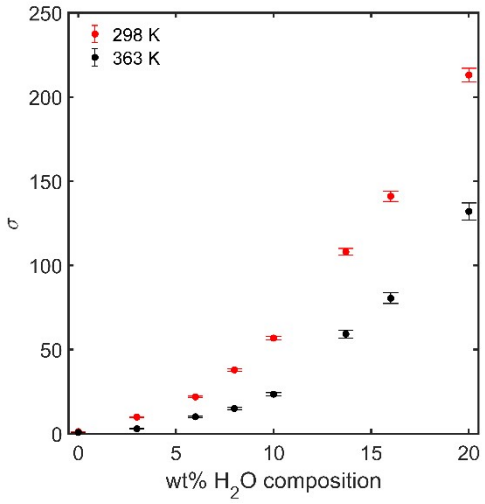

S9 - The ionic conductivity σ at temperatures of 298 K and 363 K for different wt% H_2O content, obtained from Davidson-Cole modelling the frequency dependent complex permittivity. The reduced values at the higher temperature is due to the reduced ionic mobility, owing to a reduced ionic scattering time.

5. Mn Saturation Studies

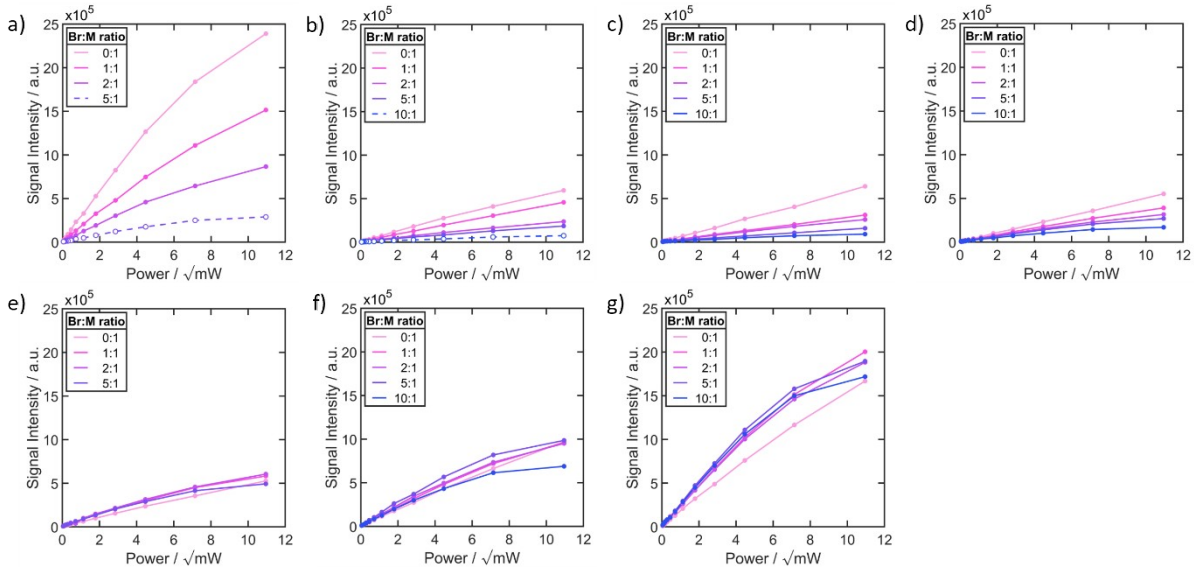

S10 – CW X-band EPR microwave power saturation studies recorded at 363K for Mn/Co/Br in varying wt% H_2O compositions, where a) 0 wt%, b) 3 wt%, c) 6 wt%, d) 10 wt%, e) 13.7 wt%, f) 16 wt% and g) 20 wt% H_2O content. Dashed lines represent samples where not all of the NaBr was dissolved.

Microwave power saturation studies on varying Br:M ratios in different H_2O/AcOH solvent compositions show the dependence of the saturation profiles of the Mn^{2+} centre on the Br concentration. The largest Br-Mn interaction can be observed at 0 wt% H_2O in the solvent (S9a), which is comparable to the interaction seen between Br-Co in the UV-vis measurements (Fig. 3 in main text), where the Mn^{2+} signal amplitude gradually decreases with increasing Br^- concentration. This corresponds to the formation of a fine white precipitate under conditions where the H_2O wt% content is very low and NaBr concentration is very high. It is therefore suggested that at lower H_2O wt% content, Br coordinates to the Mn^{2+} as well as the Co^{2+} centres. Similar interactions are seen at higher H_2O wt% content (S10a – d), however to a lesser extent, as is seen in the UV-vis measurements. We believe this to correspond to a smaller concentration of Br-Mn coordinated complex remaining in solution as the H_2O content increases. At H_2O wt% > 10 wt% (S9e - g), the signal amplitudes remain roughly constant, indicating the Br-Mn coordinated complex is no longer present, however the difference in saturation profiles with increasing Br^- concentration is still indicative of a Br-Mn interaction, potentially to a lesser extent, such as Br located in the outer coordination sphere, as is illustrated in some proposed structures in the literature.[16]

6. CW EPR at 10 K

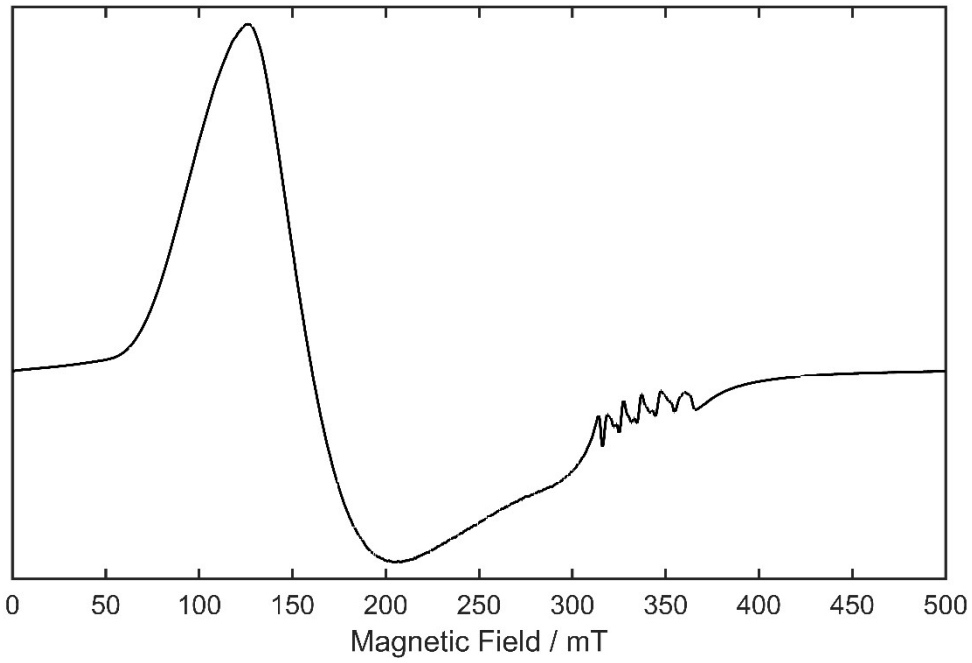

S11 – CW X-band EPR spectra of the Co/Mn/Br catalyst in 20 wt% H_2O/AcOH recorded at 4 K.

The EPR spectrum in Fig. S9 shows how the Mn^{2+} resonance around $g \sim 2$ is superimposed upon the resonance for high spin Co^{2+}, whose spectral width spans from *ca*. 60 – 400 mT. For the purpose of the ESEEM measurements designed to study only the Mn^{2+} centres of the catalyst, the Co component was omitted.

7. ESEEM

7.1 Data processing

This method of water counting in hydrated metal ions, via the detection of exchangeable ^{1}Hs, was first reported by Mims et al.[17-19] Taking the ratio of spectra recorded in protic and deuterated solvents enabled them to identify the proximity of water molecules coordinated to Cu^{2+} centres in proteins. Relative determination of ligand coordination numbers by ESEEM has also been achieved by comparison of the modulation depth of the time domain spectra.[20,21] Variations on this method have been used on systems where this method is not applicable, such as complexes with N-donor ligands, by comparison of the intensity of the double quantum (DQ) peak in the Fourier transformed (FT) data arising from the quadrupolar ^{14}N nucleus.[22] Applying these ESEEM methods to the current Co/Mn/Br based catalyst in H_2O/AcOH based solvents is challenging due to the only magnetic nuclei in the system not exhibiting DQ peaks due to the non-quadrupolar nucleus, but also having to discriminate between bulk and coordinated solvent molecules. However, a data processing procedure in which all unwanted contributions, including bulk solvent and other ligands, can be removed from the ESEEM spectrum was described by Hoogstraten and Britt[1] for a range of Mn^{2+} systems,[23-26] and this method will be employed here.

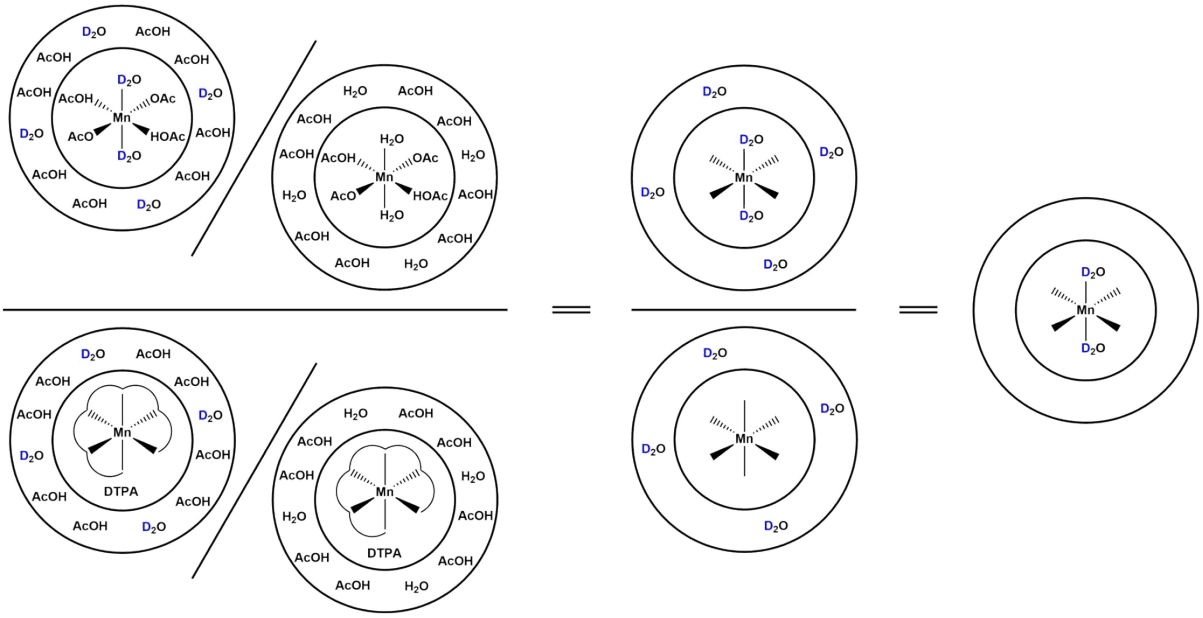

S12 – Schematic illustrating the ESEEM "Water Counting" data processing procedure adapted from Hoogstraten and Britt.[1]

The data processing procedure utilised to achieve the ESEEM data presented in Figs. 4e-h in the main text is summarised by the schematic in S11 and is adapted from Hoogstraten and Britt.[1] This illustrates how – under ^{1}H decoupling conditions – taking the ratio of ESEEM time domain data of identical samples prepared in ^{1}H and ^{2}H solvents can remove common contributions, producing data that represents purely directly coordinating H_2O ligands.

7.2 Choice of reference sample

The choice of reference sample is extremely important in order to ensure an accurate number of H_2O ligands can be determined from the modulation depth. As the modulation depth is related to both the number of nuclei n and the hyperfine coupling A, if the number of H_2O ligands in the reference is

unknown, or the A is significantly different to that of the H_2O in the analyte, then accurate modulation depth comparisons cannot be drawn.

$$k \propto n,^{1}/_{A} \qquad \text{(eq. 2)}$$

$Mn(H_2O)_6^{2+}$ was chosen as it satisfied both of these criteria. Due to the difference in the solvent systems between reference and analyte ($Mn(H_2O)_6^{2+}$ was prepared by dissolving $MnCl_2$ in H_2O), control experiments were performed to determine whether the modulation depth of the samples were effected by the quality of the glass formed at acquisition temperatures.

Typically glycerol is used as a glassing agent in aqueous solutions, however due to the natural affinity of Mn^{2+} centres for alcohol groups, it could not be used. Sucrose was utilised as an alternative glassing agent, as was also employed by Hoogstraten and Britt as the polycyclic structure has shown to be too bulky to coordinate to the metal centres.[1] Sucrose was not soluble in the H_2O/AcOH mixtures used in the Co/Mn/Br catalyst, therefore comparable amounts of glassing agent couldn't be added to both the analyte and the reference sample.

To confirm that the amount of glassing agent used did not affect the modulation depth, 1.5 and 1.9 M of sucrose was added to the $Mn(H_2O)_6^{2+}$ reference sample, shown in Fig. S12. No difference could be observed in the initial modulation depth of both samples, which was retained upon scaling to smaller n values (Fig. S13). It was therefore determined that the quality of the glass did not affect the modulation depth, and hence it was possible to compare the analyte and reference samples in different solvent systems.

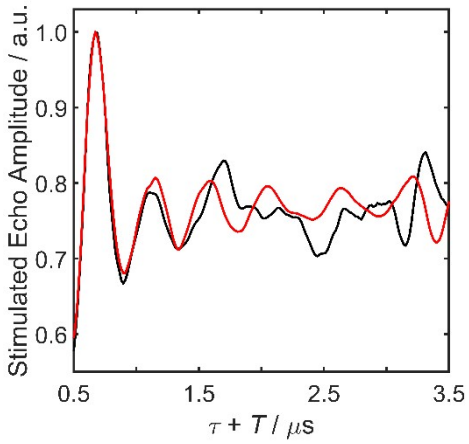

S13 - Processed 3P ESEEM spectra of $Mn(H_2O)_6^{2+}$ in H_2O with 1.5 M (black) and 1.9 M (red) of sucrose as glassing agent.

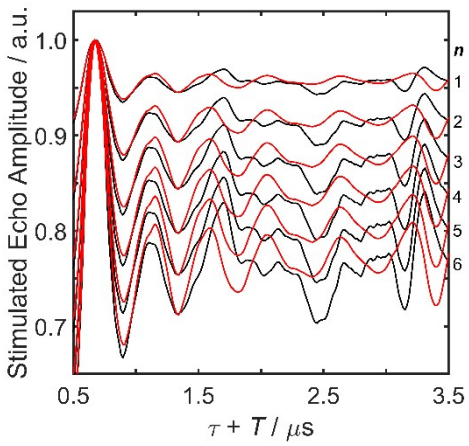

S14 - Scaled ESEEM spectra represented in S11, showing that the modulation depth between samples is consistent when scaled, where 1.5 M (black) and 1.9 M (red) of sucrose were added as glassing agent.

7.3 FSED in ^{1}H vs ^{2}H H_2O/AcOH solvent

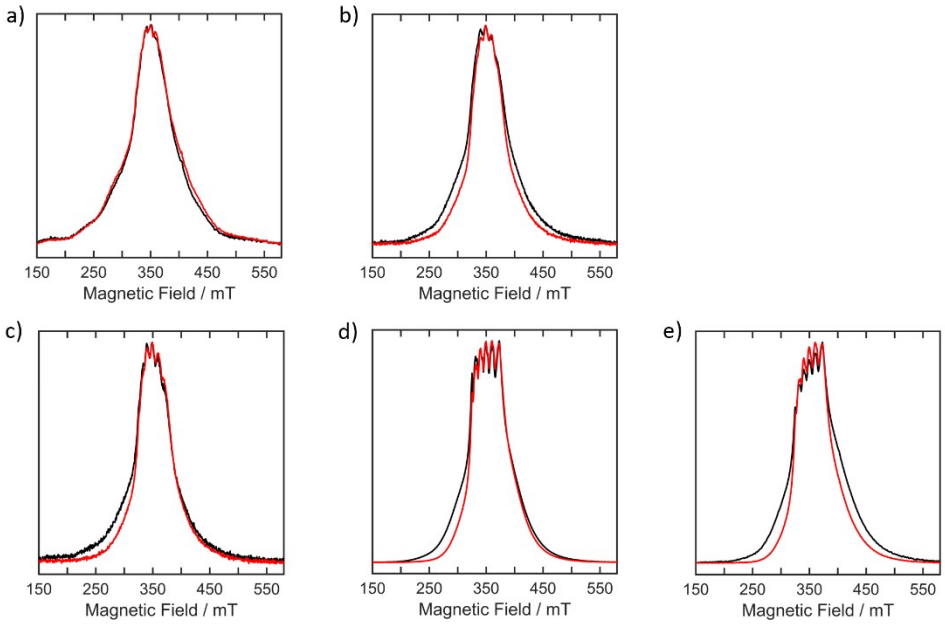

S15 – X-band FSED spectra of the Mn/Co/Br catalyst in a) 3 wt%, b) 8 wt%, c) 13.7 wt%, d) 20 wt% (D)H_2O/AcOH, and e) $Mn(H_2O)_6^{2+}$ in (D)H_2O, where D_2O (red) and H_2O (black).

The field swept echo detected (FSED) EPR spectra recorded of the Co/Mn/Br catalyst in varying (D)H_2O/AcOH ratios show a difference in the spectral width between ^{1}H and ^{2}H water in the solvent. This difference in spectral width increases with increasing (D)H_2O content in the solvent as expected, as a result of a greater (both inner and outer sphere) interaction with the Mn^{2+} nucleus.

7.4 Catalyst ESEEM processing

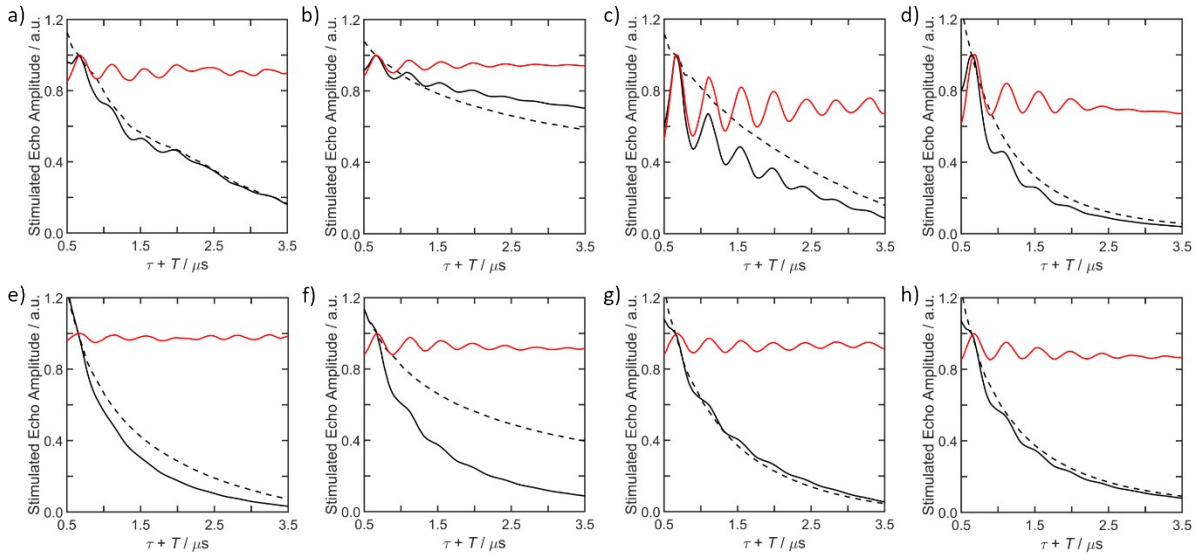

S16 – Three-pulse ESEEM time domain data and corresponding ratios for the Mn^{2+} centre in H_2O/AcOH compositions of a) 3 wt%, b) 8 wt%, c) 13.7 wt%, and d) 20 wt% H_2O content; $MnDTPA^{2+}$ centre in H_2O/AcOH compositions of e) 3 wt%, f) 8 wt%, g) 13.7 wt%, and h) 20 wt% H_2O content; where raw data for $MnCl_2$ dissolved in D_2O (solid black line), H_2O (dashed line), and D/H ratio (solid red line).

The raw data used to achieve the final ESEEM time traces shown in Fig. 4e-h in the main text are shown in Fig. S15.

A slight modulation can be seen on the ^1H curve in Fig. S15a under ^1H decoupling conditions, indicating the presence of a second magnetic nucleus coupling to the Mn^{2+} centres. Fourier transformation of this data did not allow for identification of the nucleus. However, given the low H_2O content in the solvent, and by comparison to both the UV-vis and CW EPR microwave power saturation measurements, it is likely that this is further evidence of Br interaction with the Mn^{2+}. This modulation is not observed in the final time traces in Fig. 3d due to the same principle that removes the ^2H modulations arising from the ligands.

In agreement with the results presented by Hoogstraten and Britt,[1] and by Kevan,[27] the isolated inner sphere modulation in Fig. 3c of the main text decays faster than the outer sphere modulation in the $MnDTPA^{2+}$ system due to greater anisotropy of the short range hyperfine couplings.[1] Furthermore, the time at which the stimulated echo modulation damps out completely before reappearing with inverted phase corresponds well with that observed by Hoogstraten and Britt,[1] as well as previous ^1H ENDOR data,[28,29] confirming the presence of inner sphere coordinated H_2O ligands

8 References

1 C. G. Hoogstraten and R. D. Britt, *RNA*, 2002, **8**, 252–260.
2 J. P. Grant, R. N. Clark, G. T. Symm and N. M. Spyrou, *J. Phys. E.*, 1989, **22**, 757-770.
3 A. Sulaimalebbe, A. Porch, F. J. Vidal-Iglesias and G. Attard, 2008, *MTT-S International Microwave Symposium Digest*, IEEE, Atlanta, 2008.
4 J. Barthel, K. Bachhuber, R. Buchner and H. Hetzenauer, *Chem. Phys. Lett.*, 1990, **165**, 369-373.
5 M. Tinkham, R. Weinstein and A. F. Kip, *Phys. Rev.*, 1951, **84**, 848–849.
6 G. P. Vishnevskaya and B. M. Kozyrev, *J. Struct. Chem.*, 1967, **8**, 562-568.
7 R. G. Hayes and R. J. Myers, *J. Chem. Phys.*, 1964, **40**, 877-882.
8 C. C. Hinkley and L. O. Morgan, *J. Chem. Phys.*, 1966, **44**, 898-905.
9 B. B. Garret and L. O. Morgan, *J. Chem. Phys.*, 1966, **44**, 890-897.
10 N. Bloembergen and L. O. Morgan, *J. Chem. Phys.*, 1961, **34**, 842-850.
11 N. Bloembergen, *J. Chem. Phys.*, 1957, **27**, 572–573.
12 S. Riniker, B. A. C. Horta, B. Thijssen, S. Gupta, W. F. van Gunsteren, and P. H. Hünenberger, *ChemPhysChem*, 2012, **13**, 1182-1190.
13 Lutskii, A. E., S. A. Michailenko, *J. Struct. Chem*., 1963, **4**, 14.
14 U. Kaatze, K. Menzel and R. Pottel, *J. Phys. Chem.*, 1991, **91**, 324-331.
15 D. W. Davidson and R. H. Cole, *J. Chem. Phys.*, 1950, **18**, 1417-1418.
16 W. Partenheimer, *J. Mol. Catal. A Chem.*, 2001, **174**, 29-33.
17 J. Zweier, P. Aisen, J. Peisach and W. B. Mims, *J. Biol. Chem.*, 1979, **254**, 3512–3515.
18 J. L. Zweier, J. Peisach and W. B. Mims, *J. Biol. Chem.*, 1982, **257**, 10314–10316.
19 W. B. Mims, J. Peisach and J. L. Davis, *J. Chem. Phys.*, 1977, **66**, 5536–5550.
20 D. W. Randall, A. Gelasco, M. T. Caudle, V. L. Pecoraro and R. D. Britt, *J. Am. Chem. Soc.*, 1997, **119**, 4481–4491.
21 P. C. Kang, G. R. Eaton and S. S. Eaton, *Inorg. Chem*., 1994, **33**, 3660–3665.
22 K. I. Silva, B. C. Michael, S. J. Geib and S. Saxena, *J. Phys. Chem. B*, 2014, **118**, 8935–8944.
23 L. Tao, T. A. Stich, C. N. Butterfield, C. A. Romano, T. G. Spiro, B. M. Tebo, W. H. Casey and R. D. Britt, *J. Am. Chem. Soc.*, 2015, **137**, 10563–10575.
24 D. M. Gagnon, M. B. Brophy, S. E. J. Bowman, T. A. Stich, C. L. Drennan, R. D. Britt and E. M. Nolan, *J. Am. Chem. Soc.*, 2015, **137**, 3004–3016.
25 J. Kim, S. Park, Y. K. Go, K. Jin, Y. Kim, K. T. Nam and S. H. Kim, *Inorg. Chem.*, 2020, **59**, 8846–8854.
26 M. Vogt, S. Lahiri, C. G. Hoogstraten, R. D. Britt and V. J. DeRose, *J. Am. Chem. Soc.*, 2006, **128**, 16764–16770.
27 L. Kevan, in *Time domain electron spin resonance*, eds. L. Kevan and R. N. Schwartz, Wiley-Interscience, New York, 1979, pp. 279–341.
28 K. Keller, M. Zalibera, M. Qi, V. Koch, J. Wegner, H. Hintz, A. Godt, G. Jeschke, A. Savitsky and M. Yulikov, *Phys. Chem. Chem. Phys.*, 2016, **18**, 25120–25135.
29 X. Tan, M. Bernardo, H. Thomann and C. P. Scholes, *J. Chem. Phys.*, 1993, **98**, 5147–5157.